Monthly Notices of the ROYAL ASTRONOMICAL SOCIETY

MNRAS **545,** 1–15 (2026) https://doi.org/10.1093/mnras/staf2021
Advance Access publication 2025 November 14

EP250207b is not a collapsar fast X-ray transient. Is it due to a binary compact object merger?

P. G. Jonker,[1,2★] A. J. Levan,[1,3] Xing Liu,[4] Dong Xu,[4] Yuan Liu,[4] Xinpeng Xu,[4,5] An Li,[6] N. Sarin,[7,8] N. R. Tanvir,[9] G. P. Lamb,[10] M. E. Ravasio,[1] J. Sánchez-Sierras,[1] J. A. Quirola-Vásquez,[1] B. C. Rayson,[9] J. N. D. van Dalen,[1] D. B. Malesani,[1,11,12] A. P. C. van Hoof,[1] F. E. Bauer,[13] J. Chacón,[14] S. J. Smartt,[15,16] A. Martin-Carrillo,[17] G. Corcoran,[17] L. Cotter,[17] A. Rossi,[18] F. Onori,[19] M. Fraser,[17] P. T. O'Brien,[9] R. A. J. Eyles-Ferris,[9] J. Hjorth,[20] T.-W. Chen,[21] G. Leloudas,[22] L. Tomasella,[23] S. Schulze,[24] M. De Pasquale,[25] F. Carotenuto,[26] J. Bright,[15,27] Chenwei Wang,[28] Shaolin Xiong,[28] Jinpeng Zhang,[28] Wangchen Xue,[28] Jiacong Liu,[28] Chengkui Li,[28] D. Mata Sánchez[29,30] and M. A. P. Torres[29,30]

Affiliations are listed at the end of the paper

Accepted 2025 November 4. Received 2025 November 1; in original form 2025 August 15

ABSTRACT

Fast X-ray transients (FXTs) are short-lived extragalactic X-ray sources. Recent progress through multiwavelength follow-up of *Einstein Probe*-discovered FXTs has shown that several are related to collapsars, which can also produce γ-ray bursts (GRBs). In this paper, we investigate the nature of the FXT EP250207b. The Very Large Telescope/Multi Unit Spectroscopic Explorer spectra of a nearby (15.9 kpc in projection) lenticular galaxy reveal no signs of recent star formation. If this galaxy is indeed the host, EP250207b lies at a redshift $z = 0.082$, implying a peak observed absolute magnitude for the optical counterpart of $M_{r'} = -14.5$. At the time when supernovae (SNe) would peak, it is substantially fainter than all SN types. These results are inconsistent with a collapsar origin for EP250207b. The properties favour a binary compact object merger-driven origin. The X-ray, optical, and radio observations are compared with predictions of several types of extragalactic transients, including afterglow and kilonova models. The data can be fitted with a slightly off-axis viewing angle afterglow. However, the late-time ($\sim$30 d) optical/near-infrared counterpart is too bright for the afterglow and also for conventional kilonova models. This could be remedied if that late emission is due to a globular cluster or the core of a (tidally disrupted) dwarf galaxy. If confirmed, this would be the first case where the multiwavelength properties of an FXT are found to be consistent with a compact object merger origin, increasing the parallels between FXTs and GRBs. We finally discuss whether the source could originate in a higher redshift host galaxy.

Key words: stars: black holes – stars: individual: EP250207b – supernovae: general – transients: supernovae.

1 INTRODUCTION

The first clear extragalactic fast X-ray transients (FXTs) were detected serendipitously (A. M. Soderberg et al. 2008; P. G. Jonker et al. 2013; F. E. Bauer et al. 2017). Systematic searches through *Chandra* and *XMM–Newton* archival data revealed $\approx$30 extragalactic FXTs (A. Glennie et al. 2015; D. Lin, J. Irwin & E. Berger 2019; Y. Q. Xue et al. 2019; D. Alp & J. Larsson 2020; J. Quirola-Vásquez et al. 2022, 2023; D. Eappachen et al. 2023). A small number of events later turned out to be caused by stellar flares from active stars in our Milky Way (e.g. D. Eappachen et al. 2024 reclassified the *XMM–Newton*-discovered event XRT 140811 as a stellar flare). However, for the vast majority of identified extragalactic FXTs, this scenario can be excluded. Nevertheless, without the detection of a contemporaneous counterpart at optical or near-infrared (NIR) wavelengths, their origin is difficult to determine.

A small but critically important fraction of the observed sources in the transient sky are powered by the action of a compact central engine (black hole or highly magnetic neutron star). The prototype of these extreme events is the large population of γ-ray bursts (GRBs), whose nature has been the subject of intense study in the 50 yr since their discovery. GRBs have typical durations spanning from a fraction of a second (short GRBs), to minutes (long GRBs; C. Kouveliotou et al. 1993), with only a tiny minority having durations up to a few hours (so-called ultra-long GRBs; A. J. Levan et al. 2014). They originate during the final moment of a star, via either the collapse of a massive stellar core (e.g. a collapsar; J. Hjorth et al. 2003; K. Z. Stanek et al. 2003) or the merger of two compact objects (e.g. E. Berger, W. Fong & R. Chornock 2013; N. R. Tanvir et al. 2013; B. P. Abbott et al. 2017). Whereas initially long GRBs were exclusively associated with collapsars and short GRBs with binary compact object mergers, recent results show that the long-short–collapsar-merger dichotomy is not strict (e.g. J. C. Rastinejad et al. 2022).

Using the often arcsecond-precision knowledge of the FXT X-ray source position on the sky, deep searches reveal candidate host

★ E-mail: p.jonker@astro.ru.nl

galaxies (e.g. D. Lin et al. 2022; D. Eappachen et al. 2024; J. Quirola-Vásquez et al. 2025a). This in turn allows a (photometric) redshift to be derived, which sets the luminosity and energy scales involved, crudely constraining the nature of the FXT. However, it is only since the launch of the *Einstein Probe* (*EP*) satellite (W. Yuan et al. 2022, 2025) on 2024 January 9, which is detecting about 80 FXTs per year [depending on the signal-to-noise ratio (SNR) limit adopted] and announcing their discovery rapidly, that multiwavelength counterparts to the FXTs have been discovered regularly (e.g. J. H. Gillanders et al. 2024; A. Aryan et al. 2025; X. Liu et al. 2025c; J. A. Quirola-Vasquez et al. 2025b). The follow-up observations of counterparts led to the discovery of a broad-lined Type Ic supernova (SN) in the spectra and light curve of several *EP*-discovered FXTs, in particular, EP240414a (S. Srivastav et al. 2025; H. Sun et al. 2025; J. N. D. van Dalen et al. 2025), EP250108a (R. A. J. Eyles-Ferris et al. 2025; J. C. Rastinejad et al. 2025; G. P. Srinivasaragavan et al. 2025), EP250304a (Cotter et al., in preparation), and possibly EP241021a (M. Busmann et al. 2025; G. Gianfagna et al. 2025; M. Yadav et al. 2025; J.-H. Zheng et al. 2025b; Quirola-Vasquez et al. 2025c).Similarly, for some 20–30 per cent of FXTs, a (long) GRB is detected (e.g. A. J. Levan et al. 2025; Y. Liu et al. 2025a; Y.-H. I. Yin et al. 2024; S.-Q. Jiang et al. 2025), indicating that a significant fraction of the *EP*-discovered FXTs have a collapsar origin.

However, for an important fraction of *EP*-discovered FXTs, no contemporaneous co-spatial burst of γ-ray emission is detected (M. E. Ravasio et al. 2024, 2025a, b, to list but a few) despite observations with sufficient sensitivity to detect such bursts for typical GRB spectral shapes. As several *EP*-discovered collapsar FXTs were also not detected in γ-rays, this is by no means evidence for a different nature than a collapsar origin for a significant fraction of FXTs. However, the FXT EP240408a does not seem to originate from a collapsar (W. Zhang et al. 2025a).

By analogy with the merger-driven and collapsar-driven origins of GRBs, one could wonder whether a fraction of FXTs can be linked to merger-driven events, as has been suggested for many *Chandra*-discovered FXTs, for instance on account of the plateau found in the X-ray light curve (e.g. B. Zhang 2013; B. D. Metzger & A. L. Piro 2014; R. Ciolfi 2016; H. Sun, B. Zhang & H. Gao 2017; H. Sun et al. 2019; Y. Q. Xue et al. 2019; J. Quirola-Vásquez et al. 2024). With this in mind, we report here on the *EP* X-ray discovery of FXT EP250207b and our X-ray, optical, NIR, and radio follow-up observations.

Throughout this work, we assume the spatially flat six-parameter Lambda cold dark matter Planck cosmology (Planck Collaboration VI 2020) with $H_0 = 67.7$ km s^{-1} Mpc^{-1} and $\Omega_m = 0.31$. We provide all magnitudes in the AB magnitude system. For NIR magnitudes calibrated to the Two Micron All-Sky Survey (2MASS), which is in the Vega system, we use the Vega to AB conversions $J_{\rm AB} = J_{\rm VEGA} + 0.91$, $H_{\rm AB} = H_{\rm VEGA} + 1.39$, $K_{s,\rm AB} = K_{s,\rm VEGA} + 1.85$ (M. R. Blanton & S. Roweis 2007).

2 OBSERVATIONS AND RESULTS

2.1 *Einstein Probe* X-ray observations

2.1.1 EP-Wide-field X-ray Telescope observations

A new FXT was discovered in *EP*-Wide-field X-ray Telescope (*EP*-WXT) observations on 2025 February 7, at T_0 = 21:47:56 (UTC), which lasted more than 120 s and had a reported WXT position of right ascension (RA) = 167.495 deg (J2000), and Declination (Dec.) = −7.906 deg (J2000) with a 90 per cent confidence uncertainty of 2.7 arcmin in radius (X. Y. Zhou et al. 2025). After background subtraction, 27 source photons were detected in the 0.5–4 keV energy band. See Fig. 1 for the light curve. Requiring that each bin contains one or more photons and applying Poisson statistics in the fit, the average *EP*-WXT 0.5–4 keV spectrum during this period can be fitted well [Cash statistics (W. Cash 1979), 24.5 for 24 degrees of freedom (d.o.f.)] by an absorbed power law with a (fixed; HI4PI Collaboration 2016) line-of-sight Galactic equivalent hydrogen column density of 4×10^{20} cm^{-2} and a photon index of 0.5 ± 0.7. The average unabsorbed 0.5–4 keV flux is $(6.5 \pm 3.6) \times 10^{-10}$ erg cm^{-2} s^{-1} (90 per cent confidence level). See Fig. 2 for the best fit to the *EP*-WXT X-ray spectrum. The *EP* X-ray data were processed using a data reduction pipeline and the calibration data base (CALDB) specifically designed for WXT (Liu et al., in preparation). The CALDB incorporates results both from on-ground and in-orbit calibration observations (H. Cheng et al. 2024). We used XSPEC version 12.15.0 for the fit (K. A. Arnaud 1996).

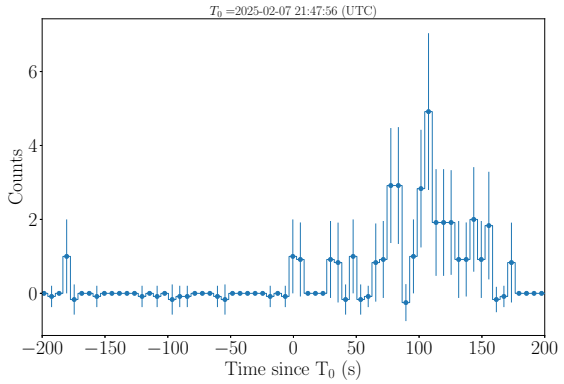

Figure 1. The background-subtracted EP250207b discovery light curve obtained by the *EP*-WXT instrument. Time is in seconds after T_0 and the bin size is 6 s. A period of ≈200 s before the FXT start is shown to assess the number of events at the source location before the FXT onset.

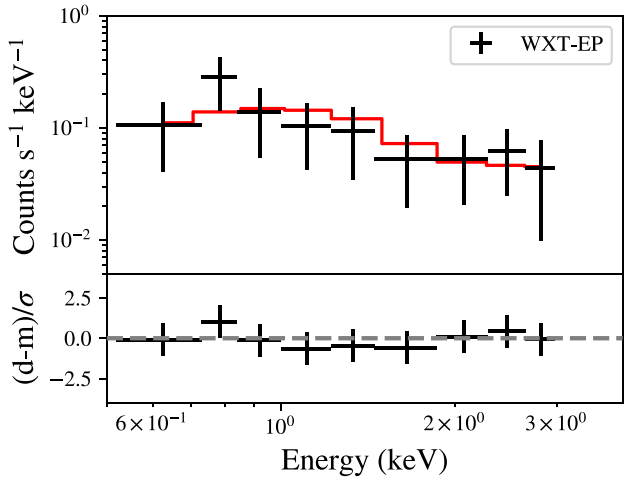

Figure 2. *Top panel*: The EP250207b discovery spectrum (0.5–4 keV) obtained by the *EP*-WXT instrument averaged over 120 s. The best-fitting power-law model affected by Galactic extinction is shown. *Bottom panel*: The data, minus the best-fitting model, divided by the error in the data point are shown. No significant deviations with respect to the best-fitting model are present.

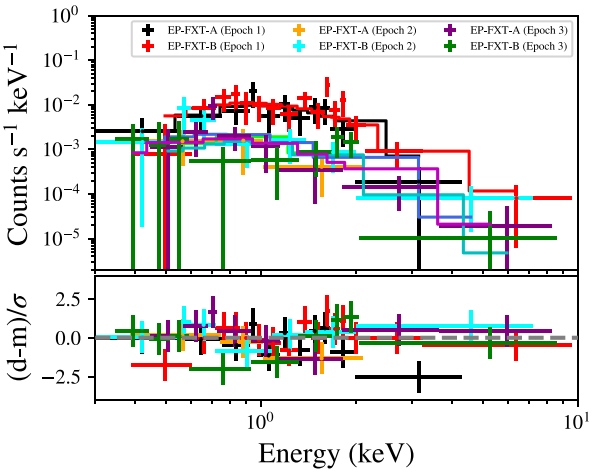

Figure 3. *Top panel*: Shown is the *EP*-FXT spectrum for each of the three observations for each FXT telescope unit A and B separately. In addition, the best-fitting power-law model affected by Galactic extinction is shown using a matching-colour drawn line. Epoch 1 *EP*-FXT-A is shown in black and *EP*-FXT-B in red, while Epoch 2 *EP*-FXT-A is shown in green and *EP*-FXT-B in blue, and finally, Epoch 3 *EP*-FXT-A is shown in light blue and *EP*-FXT-B in purple. No large change in the source spectral shape is observed in between the three observing epochs while the flux decreased between the first and the second epoch. *Bottom panel*: The data, minus the best-fitting model, divided by the error in the data are shown for each of the *EP*-FXT-A and B unit telescope–detector systems for each of the three observing epochs. No significant deviations with respect to the best-fitting model are present. The colours represent the same data/epoch as in the *top panel.*

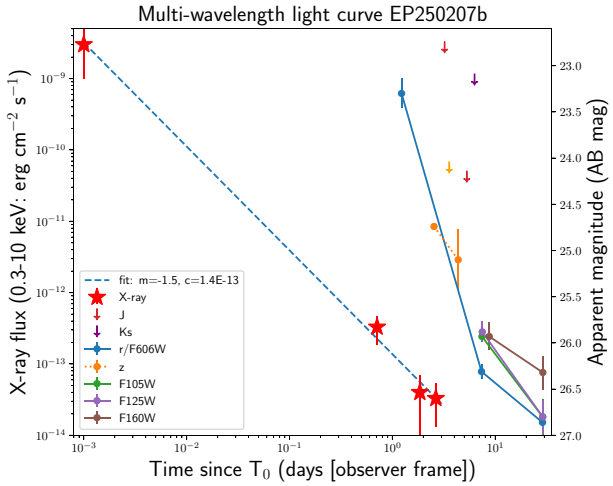

Figure 4. The *EP* 0.3–10 keV X-ray light curve of EP250207b. The first data point is the *EP*-WXT average flux and the next three data points are from the *EP*-FXT observations. The blue dashed line indicates the best-fitting power-law function of $F_X = C \times (\frac{t}{1\,\mathrm{d}})^m$. The location of the first data point is taken to be at $t = 10^{-3}$ d (≈86 s), reflecting that the first data point is an average over ≈150 s. The right-hand *y*-axis shows the observed optical and NIR magnitudes. Clear fading is detected in the different filters (see Sections 2.3 and 2.4).

2.1.2 *EP-Follow-up X-ray Telescope observations*

The *EP*-Follow-up X-ray Telescope instrument with acronym *EP*-FXT[1] consists of two telescopes, each with its own detector, systems A and B, and the detectors are sensitive over the 0.3–10 keV band. Three *EP*-FXT follow-up observations were performed. The first one started on 2025 February 8, at 14:50:57 (UTC) with an exposure time of 3025 s (at $t = 0.71$ d after the *EP*-WXT trigger). The second one started on 2025 February 9, at 18:09:49 (UTC) with an exposure time of 5044 s (at $t = 1.85$ d after the *EP*-WXT trigger). The results of these first two observations have also been announced in X. Y. Zhou et al. (2025) with a best-fitting source J2000 position of (RA, Dec.) = (167.5130, −7.8695) with an uncertainty of 10 arcsec (radius, 90 per cent confidence level). A third observation started on 2025 February 10, at 13:16:43 (UTC) with an exposure time of 9045 s (at $t = 2.65$ d after the *EP*-WXT trigger).

The spectra of these *EP*-FXT observations (see Fig. 3) have been fitted simultaneously using an absorbed power law with a Galactic equivalent hydrogen column density fixed to the mean line-of-sight value provided in HI4PI Collaboration (2016) of 4×10^{20} cm^{-2} and photon indices of 1.6 ± 0.4, 2.3 ± 0.9, and 2.3 ± 0.9 for the first, second, and third observations, respectively. In the fit, the *EP*-FXT-A and *EP*-FXT-B detectors have their own response matrices. The fit has a Cash statistic of 156 for 147 d.o.f. The unabsorbed 0.3–10 keV fluxes are $(3.3^{+1.4}_{-0.9}) \times 10^{-13}$, $(4^{+3}_{-1}) \times 10^{-14}$, and $(3^{+2}_{-1}) \times 10^{-14}$ erg cm^{-2} s^{-1} (90 per cent confidence level), respectively. No significant change in the power-law spectrum is observed over the three observing epochs while the flux decreased, at least between the first and second epochs. We also investigated the data of the *EP*-FXT-A and *EP*-FXT-B detectors for each of the three epochs to search for variability (e.g. flares), but none were found. Note that each detector only detected between 17 and 61 counts during these observations.

We converted the 0.5–4 keV *EP*-WXT (unabsorbed) flux to a 0.3–10 keV (unabsorbed) flux to facilitate comparison with the *EP*-FXT unabsorbed flux using the web-based, portable, interactive, multi-mission simulator (W3PIMMS) taking the best-fitting absorbed power-law model to the *EP*-WXT spectrum (see Section 2.1.1) as input. We obtain an *EP*-WXT unabsorbed 0.3–10 keV flux of $(3^{+2}_{-1.4}) \times 10^{-9}$ erg cm^{-2} s^{-1}. We show the X-ray light curve combining the *EP*-WXT and *EP*-FXT measurement in Fig. 4. Overplotted is the best-fitting power-law decay function with $F_X = C \times (\frac{t}{1\,\mathrm{d}})^m$, the best-fitting power-law index $m = -1.5$, and $C = 1.4 \times 10^{-13}$ erg cm^{-2} s^{-1}.

2.2 GECAM limits on γ-ray emission

The Gravitational wave high-energy Electromagnetic Counterpart All-sky Monitor (GECAM) is a constellation of four γ-ray all-sky monitors, including GECAM-A/B (X. Q. Li et al. 2022), GECAM-C (D. Zhang et al. 2023), and GECAM-D (C. Wang et al. 2024). Throughout the burst duration of EP250207b, only GECAM-B was continuously collecting data with a good coverage of the location of EP250207b. However, no significant signal was detected neither in-flight (X.-Y. Zhao et al. 2024) nor on-ground (C. Cai et al. 2025). We performed a targeted search (C. Cai et al. 2021) for the detection of a source using GECAM-B data from 2025-02-07 21:47:36 to 2025-02-07 21:56:16 (UTC). No significant source is found. We calculated an upper limit to the detection of a source considering three typical GRB spectral models [i.e. soft, normal, and hard Band functions (following e.g. C. Zheng et al. 2025a) and three time-scales (0.1 s, 1 s, 10 s)]. The 3σ upper limits (Y.-Q. Zhang et al. 2025b) on the GRB flux (10–1000 keV) vary in the range $\approx(1-10) \times 10^{-7}$ erg cm^{-2} s^{-1} for the longest hard to the shortest soft assumed GRBs. We also checked for a potential γ-ray counterpart of EP250207b in the *Fermi* Gamma-ray

[1]Note that we always refer to the *EP* Follow-up X-ray Telescope instrument as '*EP*-FXT' and to a fast X-ray transient as 'FXT' to try to avoid confusion between the two.

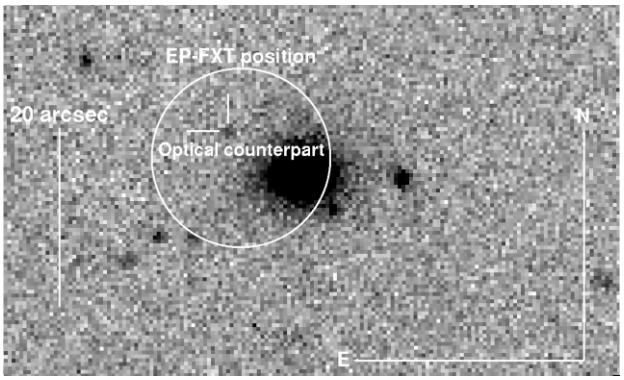

Figure 5. The NOT/ALFOSC discovery r'-band image of the optical counterpart to the FXT EP250207b combining the two best-seeing images of the four. The white circle indicates the *EP*-FXT source localization uncertainty region (X. Y. Zhou et al. 2025). The new faint optical source ($r' = 23.3 \pm 0.16$ mag) is indicated by the tick marks. It lies in projection close to the galaxy WISEA J111002.65−075211.9.

Burst Monitor (GBM) instrument data. Unfortunately, the location of the source was Earth-occulted for *Fermi*/GBM for the entire duration of the event, so no simultaneous *Fermi*/GBM upper limit can be reported. Finally, we checked whether the EP250207b location was observed by *Swift*/BAT. While the location of the source was not Earth-occulted for the *Swift* Burst Alert Telescope (BAT) instrument, the position fell outside the coded-mask field of view. As a result, we do not report a *Swift*/BAT upper limit.

2.3 Optical and near-infrared ground-based observations

The photometry reported below is uncorrected for extinction, which taking the $N_{\rm H} = 4 \times 10^{20}$ cm^{-2} from the X-ray spectral fits, would correspond to an $A_V = 0.18$ mag following T. Güver & F. Özel (2009). This is slightly higher than the Galactic $A_V = 0.14$ mag derived from the dust reddening in stars detected in the Sloan Digital Sky Survey (SDSS) [E. F. Schlafly & D. P. Finkbeiner 2011, assuming $\frac{A_V}{E(B-V)} = 3.1$]. Given the intrinsic scatter in the relation, this is likely consistent with the Galactic A_V value (cf. H. Zhu et al. 2017).

2.3.1 NOT/ALFOSC + NOT/NOTCam

The field of EP250207b was observed twice using the Nordic Optical Telescope (NOT). Initially, the Alhambra Faint Object Spectrograph and Camera (ALFOSC) instrument was used to obtain four exposures of 200 s in the r' filter. The mid-time of these exposures was 2025-02-09 03:16:13 UTC, i.e. 1.23 d after the *EP*-WXT start time of EP250207b. After standard bias subtraction and correction for flat-field, a source was discovered that is not present in deeper Legacy Survey images (A. Dey et al. 2019) of the field. We subtract the Legacy r'-band image from the new NOT image to remove background light at the position of the counterpart due to the nearby (candidate host) galaxy using the ZOGY algorithm (B. Zackay, E. O. Ofek & A. Gal-Yam 2016) implemented in PyZOGY (D. Guevel et al. 2021). From the subtracted image, we obtain a magnitude of $r' = 23.3 \pm 0.16$ for the new source (calibrated against stars detected in the Panoramic Survey Telescope and Rapid Response System [Pan-STARRS] catalogue). This is broadly consistent with the magnitude of $r' \approx 23.7$ quoted in the original work reporting on these data (X. Liu et al. 2025b). In Fig. 5, we show the NOT counterpart r'-band discovery image.

At a mid-time of 2025-02-11 03:07:13 UTC, i.e. 3.22 d after the onset of the FXT, 30 exposures of 60 s each were obtained in the J-band filter using the NOTCam detector. No source was detected in the combined image at the location of the candidate optical counterpart to the FXT down to $J_{\rm AB} > 22.8$ mag (3σ).

In order to determine the best position of the source, we combined the first and last of our four ALFOSC images as they were taken under the best seeing conditions. The best-fitting position of the transient source has an RA (J2000) = 11:10:03.22 and Dec. (J2000) = −07:52:07.25 with an estimated uncertainty of ≈0.5 arcsec (68 per cent confidence), which falls well inside the *EP*-FXT error region of EP250207b (see Fig. 5).

2.3.2 Gemini North and South Multi-Object Spectrograph observations

The field of the FXT was observed using the Gemini Multi-Object Spectrograph (GMOS), on both the Gemini-South (GS) telescope located at Cerro Pachon, Chile, as well as the Gemini-North (GN) telescope located at Mauna Kea, Hawaii, U.S. GMOS was used in imaging mode during three epochs [two at GN at ∼2.54 d (6 exposures of 60 s each) and 3.57 d (5 exposures of 60 s each), and one at GS 4.36 d after the discovery of EP250207b (12 exposures of 60 s each) using programmes GS-2024B-Q-131 and GS-2024B-FT-112 (PI Bauer)]. Two GMOS observations were executed using the z' filter and one using the g' filter. In the first GMOS observation, a faint source was detected at the position of the candidate optical counterpart with $z' = 24.7 \pm 0.2$ mag. The second z'-filter observation yielded a non-detection with $z' > 24.1$ mag, while a deeper final GS/GMOS observation provided a faint detection with $z' = 25.1 \pm 0.3$ mag. The photometry was calibrated against Pan-STARRS.

Furthermore, we used the FLoridA Multi-object Imaging Near-infrared Grism Observational Spectrometer 2 (FLAMINGOS 2; a.k.a. F2) mounted on GS at two different epochs to observe the field of EP250207b in the J and K_s filters. The J-band observations were obtained on 2025-02-13, the first and last exposures started at 04:46:41 (UTC) and 05:12:35 (UTC), respectively. We combined 27 exposures of 40 s to search for emission from the counterpart. No source was detected at the position of the counterpart, with a 3σ upper limit of $J_{\rm AB} > 24.2$ mag using the Photometry Sans Frustration PYTHON tool (M. Nicholl et al. 2023). In addition, on 2025-02-14 starting at 04:39:23 (UTC), 90 exposures of 15 s each were obtained using the K_s filter. The last exposure started at 05:33:11 (UTC). We derive an upper limit at the source position of $K_{s,\rm AB} > 23.15$ mag (3σ).

2.4 *Hubble Space Telescope* observations

The field of the optical counterpart to EP250207b was observed twice using the Wide Field Camera 3 (WFC3) onboard the *Hubble Space Telescope* (*HST*) under programme GO-17806 (PI Tanvir). Observations were obtained in four different wide-band filters and two detectors. During the first epoch, 4 × 505 s exposures were obtained totalling 2020 s in the *F*606*W* filter using the ultraviolet-visible (UVIS) detector and 4 exposures of 552.94 s were obtained totalling ≈2212 s in *F*105*W*, *F*125*W*, and *F*160*W*, each was obtained using the infrared (IR) detector. All the second-epoch observations had an identical set-up and exposure time as that of the first epoch. However, during the second epoch of *F*606*W* observations, a cosmic ray hit very close to the transient's position was present in two of the four exposures. Therefore, we used only 2 × 505 s totalling 1010 s of exposure in the *F*606*W* filter.

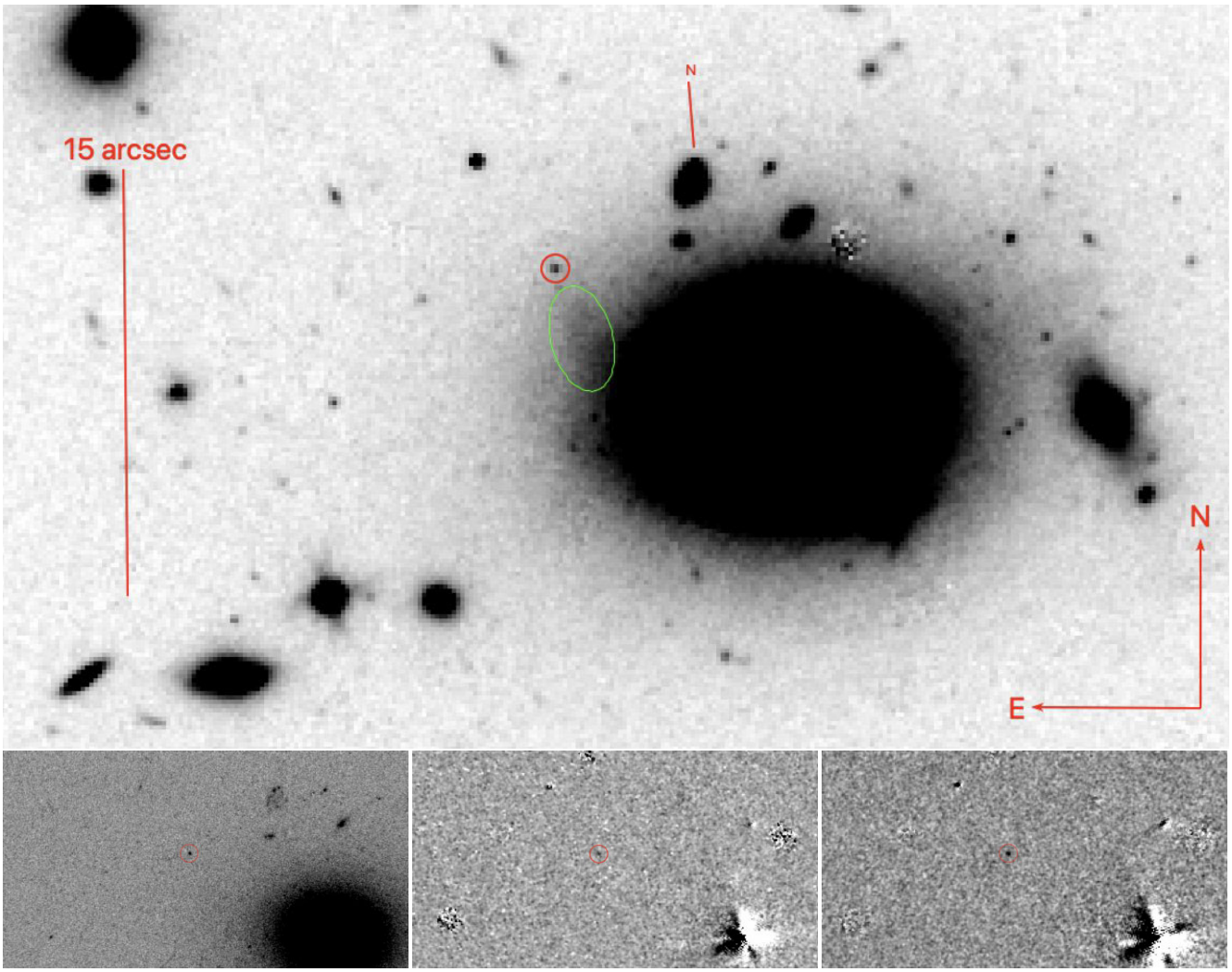

Figure 6. *Top panel*: First and second epochs of our *HST* WFC3 $F606W + F105W + F125W + F160W$ filters' observations of the field of EP250207b combined. The red circle shows the location of the transient first identified in our NOT observations. In addition, a galaxy to the north of the lenticular galaxy is indicated with 'N'. This galaxy has a redshift $z = 2.18$ (see text). The figure also clearly shows the proximity of the optical counterpart of EP250207b to the candidate (lenticular) host galaxy WISEA J111002.65−075211.9 at $z = 0.082$. Finally, an overdensity of stars seemingly connecting the lenticular galaxy with the location of the transient is indicated with a green ellipse to guide the eye. *Bottom left panel*: First epoch of our *HST* WFC3 $F606W$ filter observations of the field of EP250207b, showing the location of the transient first identified in our NOT observations at a magnitude of $F606W = 26.31 \pm 0.08$, to be compared with the $r' = 23.3$ band magnitude at detection. *Bottom middle panel*: The residual image resulting from subtracting the second epoch of our *HST* WFC3 $F105W$ filter observation from the first. In the region indicated by the red circle, a positive residual is present, indicating the counterpart faded between the first and second epochs of our *HST* $F105W$ observations. *Bottom right panel*: The residual image resulting from subtracting the second epoch of our *HST* WFC3 $F125W$ filter observation from the first. The fading further solidifies the association between the counterpart and the FXT EP250207b. In all these three panels, the size of the circle is the same (0.5 arcsec) as that in the *top* panel.

The observations were taken over the periods 7.4–8.7 and 28.8–29.0 d after the WXT trigger. Images were aligned to sources in common to each frame, and subsequently drizzled to final pixel scales of 0.05 and 0.07 arcsec pixel^{-1} for the UVIS and IR filter observations, respectively. A source is detected in all *HST* filter observations in both epochs at the position of the NOT-optical counterpart. We combined all the filter observations and both epochs into a single image drizzled to a pixel scale of 0.15 arcsec (see the *top panel* of Fig. 6). An overdensity of stars seemingly connecting the lenticular galaxy with the location of the transient is found and indicated with a green ellipse to guide the eye in the figure. In addition, in Fig. 6, we show the resultant first-epoch $F606W$ image (*bottom left panel*), the difference image obtained subtracting the second-epoch $F105W$ image from the first epoch (*bottom middle panel*), and the difference image obtained subtracting the second-epoch $F125W$ image from the first epoch (*bottom right panel*).

From the difference images, it is clear that the source faded between the first and second epochs of *HST* observations in the $F105W$ and $F125W$ bands, while the magnitude measurements in the $F606W$ bands also show it faded in $F606W$. Due to the larger measurement uncertainties in the $F160W$ band observations (see Table A1), there is only marginal evidence for fading between *HST* Epoch 1 and 2 in that band. We collate all the optical and NIR photometry in Table A1 and we show the light curves in Fig. 4.

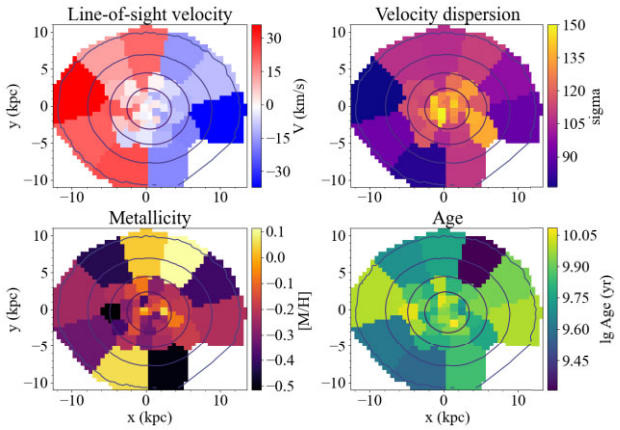

Figure 7. Spatial distributions of the line-of-sight velocity V, the velocity dispersion σ, the metallicity [M/H], and age in the 45 Voronoi bins of the candidate host galaxy WISEA J111002.65−075211.9 observed with MUSE. The axes are given in x and y distances from the central pixel of the $z = 0.082$ galaxy in kiloparsecs. Note that the location of the transients lies outside the sky region shown.

2.4.1 Very Large Telescope/MUSE

We observed the candidate host galaxy and the location of EP250207b on 2025-03-03 using the Multi Unit Spectroscopic Explorer (MUSE) mounted on Very Large Telescope (VLT) Unit Telescope 4. The observations are part of the programme with ID 111.259Q (PI Jonker) and started at 02:47:36 (UTC) and lasted until 03:50:08 (UTC). Four exposures of 697 s each were obtained with small positional offsets between the exposures; however, the seeing deteriorated significantly while the exposures were obtained. Therefore, we only used the first two exposures with the best seeing of ≈1 arcsec. The data are reduced using the European Southern Observatory (ESO) Reflex pipeline (ESO CPL Development Team 2015; P. M. Weilbacher et al. 2020).

The MUSE cube data of the candidate host galaxy are spatially Voronoi binned to a target SNR (S/N) =30 per bin using the `VorBin` method and software of M. Cappellari & Y. Copin (2003). Each spectroscopic bin in each spaxel with an S/N < 5 is rejected to remove residual-dominated spectra before binning. Out of the 46 spatial spectra, 1 is contaminated by light of an object to the south-east of the galaxy; therefore, this spatial bin is removed, leaving 45 (see Fig. 7).

The candidate host galaxy, WISEA J111002.65−075211.9 (A. J. Levan et al. 2025), is classified in the NASA/IPAC Extragalactic Database (NED) as an irregular spiral galaxy; however, in the *HST* images, it visually resembles a lenticular or elliptical galaxy. In Fig. 7, we show the spatial distributions for the radial velocity V, the velocity dispersion σ, the total metallicity [M/H], and age of the stellar population. We note that the spatial variation detected in V, shown in the top left panel of Fig. 7, is typical for that observed in a lenticular galaxy (e.g. E. Emsellem et al. 2004).

We also obtain the average spectrum of the whole galaxy combining the 45 spatial bins. We use the penalized pixel fitting method (PPXF; M. Cappellari 2017) to fit the spectrum. We use *Flexible Stellar Population Synthesis* (FSPS V3.2; C. Conroy, J. E. Gunn & M. White 2009; C. Conroy & J. E. Gunn 2010; C. Conroy, M. White & J. E. Gunn 2010) as the template bank for our stellar population synthesis model. As input parameters, we use the redshift $z = 0.082$, $v = 0$ km s^{-1} (with respect to this redshift), and stellar velocity dispersion of $\sigma = 200$ km s^{-1} as initial guesses. The best fit for the average spectrum of the galaxy is displayed in Fig. 8. The average spectrum is shown in black, with the best-fitting galaxy template overplotted in red. The residuals of the fit are shown in green.

2.5 MeerKAT radio observations

We observed the position of EP250207b with the MeerKAT radio telescope (F. Camilo et al. 2018; J. Jonas 2018), as part of programme SCI-20241101-FC-01 (PI Carotenuto). We conducted three observations log-spaced in time, each with the same total on-source time of 42 min. The first observation started on 2025 February 13 at 01:02 UTC (≈5.1 d after the first X-ray detection). The second and third observations were performed, respectively, on 2025 March 3 at 00:47 UTC (≈23 d after the first X-ray detection) and on 2025 March 23 at 00:41 UTC (≈43 d after the first X-ray detection). We observed at a central frequency of 3.06 GHz (*S* band, S4), with a total bandwidth of 875 MHz. PKS J1939–6342 and PKS 1128-047 were used as flux and complex gain calibrators, respectively. The data were reduced with the `OxKAT` pipeline (I. Heywood 2020), which performs standard flagging, calibration, and imaging using `tricolour` (B. V. Hugo

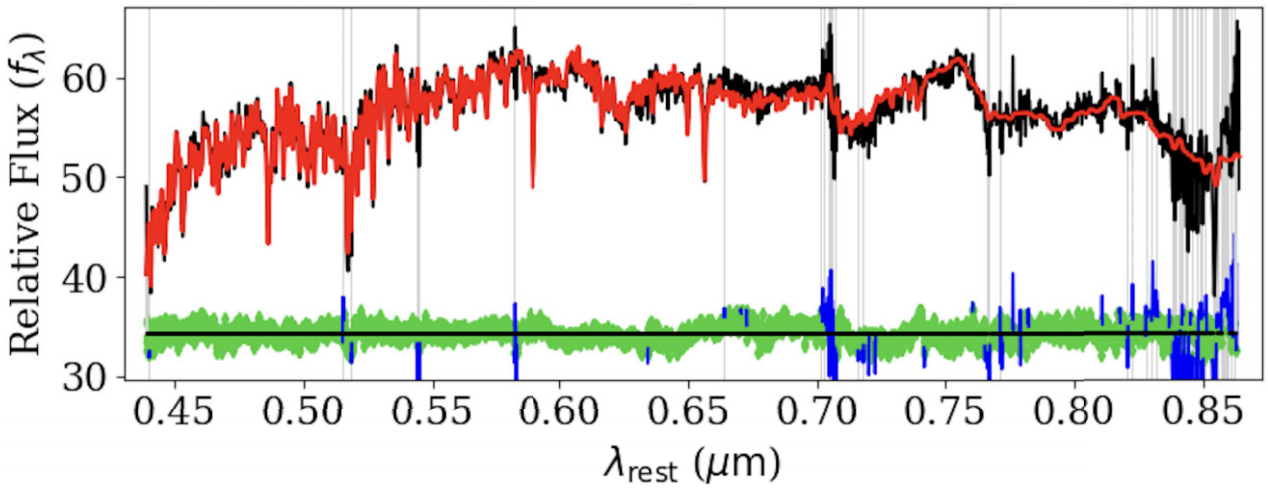

Figure 8. Best-fitting PPXF (M. Cappellari 2017) model to the MUSE spectrum of the host galaxy. The observed spectrum is shown in black, with the FSPS template in red. Model-subtracted residuals are shown in green, with blue and the grey shaded regions showing the removed outliers to the model.

et al. 2022), CASA (CASA Team et al. 2022), and WSCLEAN (A. R. Offringa et al. 2014), respectively. In the imaging step, we adopted a Briggs weighting scheme with a −0.3 robust parameter, yielding an ∼3.6 arcsec beam and an 8 μJy beam^{-1} rms noise in the target field. We do not detect radio emission at the position of the optical counterpart of EP250207b, and we place a 3σ upper limit on the peak flux density of the target at 27, 24, and 27 μJy beam^{-1}, for the first, second, and third observations, respectively. To search for persistent radio emission at the location of the source, we also stacked the data of the three epochs. No radio source was detected down to a 3σ upper limit of 15 μJy beam^{-1}.

3 DISCUSSION

After the *EP* discovery of EP250207b, we obtained X-ray, optical, NIR, and radio observations to follow the source evolution. We could not derive a direct redshift of the transient. However, the transient's location, next to the large lenticular galaxy WISEA J111002.65−075211.9, provides statistical evidence through the low $P_{\rm chance} < 0.5$ per cent (D. B. Malesani et al. 2025) for their association. Furthermore, our combined, deep, *HST* observations show that the source position is consistent with the outskirts of this galaxy (Fig. 6). This image further reveals the presence of enhanced emission seemingly bridging the lenticular galaxy and the position of the transient (see the green ellipse in the top panel of Fig. 6), further strengthening the suggested physical connection. Finally, in our deep *HST* imaging, we find no evidence for extended emission at the source position, such as could be the case had the source originated in a not-too-distant background galaxy. Therefore, we first discuss the nature and the properties of the source under the assumption that it lies at the same redshift as the lenticular galaxy ($z = 0.082$; A. J. Levan et al. 2025; and this work, see Section 2.4.1).

At a redshift $z = 0.082$, the observed brightest absolute magnitude of $r'_{\rm ABS} = -14.5$ is rather faint when compared to the peak absolute magnitude of several *EP*-discovered FXTs (e.g. see Fig. 9). However, while it is too faint to be explained as an afterglow of a long GRB, it is consistent with the peak absolute magnitude and light-curve evolution of some fainter, merger-driven short GRBs (Fig. 9). Furthermore, the offset of 10 arcsec (X. Liu et al. 2025b), corresponding to 15.9 kpc in projection, is well within the range of typical host galaxy offsets observed for short GRBs (e.g. J. S. Bloom, S. R. Kulkarni & S. G. Djorgovski 2002; W.-f. Fong et al. 2022) and simulated merger origin GRB population studies (S. Mandhai et al. 2022). In addition, the high age of the stars in the lenticular galaxy that we derive from our VLT/MUSE observations (see Fig. 7) is inconsistent with a collapsar origin, but is consistent with a merger-driven (short) GRB scenario. Finally, the rate of decay observed in the r' and $F606W$ band (see Fig. 4) seems to decelerate. This could be consistent with persistent contributions from a globular cluster or the core of a (tidally disrupted) dwarf galaxy host for EP250207b. At a redshift $z = 0.082$, a globular cluster near the peak of the absolute magnitude distribution, i.e. with an absolute magnitude of ≈−10 (W. E. Harris 2010), would correspond to $F606W = 27.84$ AB mag and thus would contribute about 30 per cent to the observed flux at our observational epoch $t \approx 28$ d. Clearly, an even brighter globular cluster could be responsible for nearly all the optical/NIR light in this final epoch. The absolute magnitude distribution of ultra-compact dwarfs (UCDs), which might be the cores of tidally disrupted dwarf galaxies, overlaps that of the bright end of the absolute magnitude distribution of globular clusters (e.g. S. Mieske, M. Hilker & L. Infante 2002), so the source observed at late time could also be explained by such a UCD. A tidal stream from a tidally disrupted dwarf galaxy could also explain

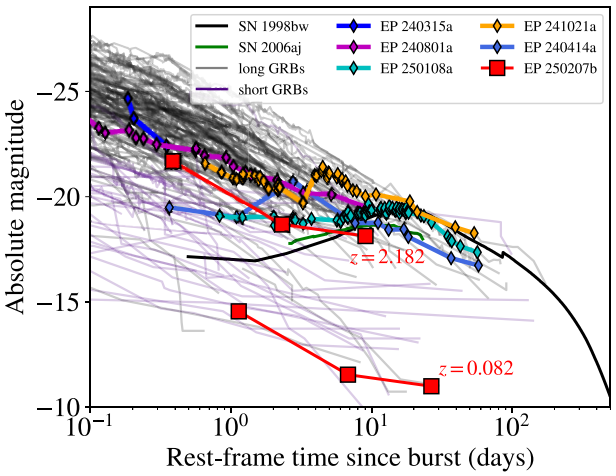

Figure 9. Kann plot showing the approximate r'-band light curve of EP250207b in red together with those of a sample of *EP*-discovered FXTs [EP240414a (blue; J. N. D. van Dalen et al. 2025), EP241021a (orange; J. A. Quirola-Vásquez et al. 2025c), EP240801 (purple; S.-Q. Jiang et al. 2025), EP240315a (dark blue; A. J. Levan et al. 2025), and EP250108a (magenta; R. A. J. Eyles-Ferris et al. 2025; J. C. Rastinejad et al. 2025)], short GRBs (thin purple lines), and long GRBs (thin black lines). The GRB light curves are obtained from D. A. Kann, S. Klose & A. Zeh (2006), D. A. Kann et al. (2010, 2011), and A. Nicuesa Guelbenzu et al. (2012). The absolute magnitudes of the data points in the light curve from EP250207b at $z = 0.082$ are consistent with the faint end of that of the short GRB distribution. If the source redshift is $z = 2.18$ instead (see Section 3), the light curve is consistent with that of the bright end of short GRBs. The evolution as a function of time is consistent with that seen in short GRBs also, although the decay rate seems to decelerate after the first *HST* observation (near $t = 7$–8 d). For a redshift $z = 0.082$, the presence of a (broad-lined) Type Ic (or indeed any) SN can be ruled out.

the enhanced emission linking WISEA J111002.65−075211.9 and the location of the transient. Future *HST* or *James Webb Space Telescope* observations of EP250207b can test the scenario that part or all of the light in the last epoch of *HST* observations is due to a globular cluster or a disrupted dwarf galaxy. Finally, for a redshift $z = 0.082$, the absolute magnitudes on rest-frame time-scales of ≈5–25 d after the discovery of EP250207b rule out the presence of a (broad-lined) Type Ic (or indeed any) SN.

The 3.06 GHz radio MeerKAT non-detections at $t = 5.6$, 23, and 43 d after the discovery at flux levels of ≈25 μJy imply a radio luminosity upper limit of $L_{3.06\ \rm GHz} \lesssim 1.3 \times 10^{37}$ erg s^{-1}, or $\lesssim 4 \times 10^{27}$ erg s^{-1} Hz^{-1}. Such a radio luminosity is low when compared to the radio emission detected for (on-axis) short GRBs (see e.g. fig. 13 in W. Fong et al. 2021). We used REDBACK (N. Sarin et al. 2024) to compare our radio, optical (r'/V-band), and X-ray light curves with those estimated via the afterglow_models.gaussian_redback structured jet model. This model is identical to that used for the only confirmed 'off-axis' viewed merger origin GRB 170817A (e.g. J. D. Lyman et al. 2018; G. P. Lamb et al. 2019), and assumes a Gaussian-shaped jet structure. The external medium of the afterglow is assumed to be uniform, and the jet undergoes sideways expansion as described by J. Granot & T. Piran (2012) for their $a = 1$ case. The model priors and posterior distributions are presented in Table 1 and the fit is indicative of a mildly 'off-axis' viewed GRB afterglow in a low-density ambient medium (see Fig. 10, and Fig. B1 for the corner plot). Note that H. C. I. Wichern et al. (2024) showed that an off-axis scenario is difficult to reconcile with the properties of the full sample of *Chandra*-discovered FXTs, suggesting perhaps

Table 1. The model parameters for our afterglow model fit data shown in Fig. 10. Note that we excluded the optical and NIR data obtained after $t > 10$ d from the fit, as this emission seems to be coming from a component that is not an afterglow. The prior range and, where appropriate, the distribution function are given (else the distribution is flat in the range indicated), and the model posterior median and $1-\sigma$ confidence interval. A corner plot of the posterior distribution is included in Appendix B.

Parameter	Prior	Posterior	Description
$\theta_{\rm observer}$ (rad)	[sin]$0 \leftrightarrow \pi/2$	0.11 ± 0.04	Observers' line-of-sight angle
$\log E_{\rm K,iso}$ (log erg)	$44 \leftrightarrow 54$	51.7 ± 0.7	Isotropic equivalent kinetic energy
$\theta_{\rm core}$ (rad)	$0.01 \leftrightarrow 0.1$	0.08 ± 0.02	Jet core half opening angle
$\theta_{\rm edge}$ (rad)	$0.1 \leftrightarrow 0.2$	0.16 ± 0.03	Angular extent of structured jet
$\log n_{\rm ism}$ (log cm^{-3})	$-5 \leftrightarrow 2$	$-4.3^{+0.8}_{-0.5}$	Ambient medium number density
p	$1.4 \leftrightarrow 3.1$	2.92 ± 0.06	Electron spectral energy density index
$\log \epsilon_e$	$-5 \leftrightarrow 0$[a]	$-0.4^{+0.2}_{-0.4}$	Fraction of energy in electrons
$\log \epsilon_B$	$-5 \leftrightarrow 0$[a]	-2.9 ± 1.4	Fraction of energy in magnetic field
ε_N	$0.1 \leftrightarrow 1.0$	$0.34^{+0.3}_{-0.17}$	Synchrotron participation fraction
Γ_0	$40 \leftrightarrow 400$	260 ± 110	Initial bulk Lorentz factor

Note. [a]We also set the requirement $\log \epsilon_e > \log \epsilon_B$.

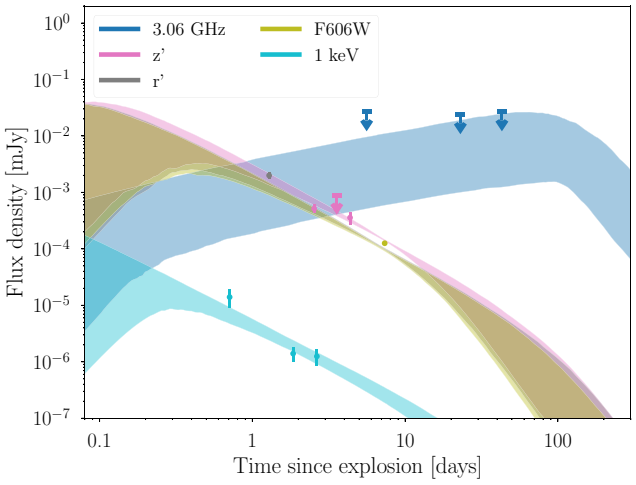

Figure 10. We used REDBACK (N. Sarin et al. 2024) to fit the optical (grey, green, and pink) and X-ray (light blue) afterglow data (excluding the data obtained after $t > 10$ d), including the radio (blue) upper limits at an assumed redshift, $z = 0.082$. The afterglow model used was gaussian_redback following G. P. Lamb, I. Mandel & L. Resmi (2018) and including synchrotron self-absorption effects (see G. P. Lamb & S. Kobayashi 2019, for details). The shaded regions indicate the 90 per cent credible interval for the model fits to the data, where we used NESSAI (M. J. Williams, J. Veitch & C. Messenger 2024) as the sampler with a Gaussian likelihood. The model fits return an out-of-jet-core viewing angle, essentially perhaps slightly 'off-axis', of $\sim 6.^{\circ}3$ for a jet core angle of $\sim 4.^{\circ}6$; however, the uncertainties on both parameters are also consistent with an 'on-axis' scenario. Furthermore, the Gaussian structured jet 'wings' extend to $\sim 9.^{\circ}2$, although the energy at the wider angles will contribute insignificantly to the observed emission. After the initial decay from the prompt emission (the prompt emission is not modelled here), the X-ray observations from *EP*-FXT, the optical/NIR data at $t < 10$ d, and radio upper limits are consistent with mildly off-axis afterglow emission.

that (some) *EP*-discovered FXTs have a different nature than those. Finally, the optical emission detected in the second *HST* epoch of observations is too bright for our afterglow model, suggesting that additional emission mechanisms or sources (such as the possible globular cluster or dwarf galaxy mentioned above) could contribute to the optical light.

The average 0.3–10 keV X-ray luminosity at the *EP*-WXT discovery is $L_{\rm X,ave} = 1 \times 10^{46}$ erg s^{-1}. This X-ray luminosity is on the high end, but still consistent with, the X-ray luminosity theorized to be emitted through the spin-down of an millisecond (ms) massive (>2 M$_\odot$) magnetar formed in a binary neutron star merger (e.g. B. Zhang 2013; B. D. Metzger & A. L. Piro 2014; R. Ciolfi 2016; H. Sun, B. Zhang & H. Gao 2017; H. Sun et al. 2019; J. Quirola-Vásquez et al. 2024). Note that under this model the X-ray emission is quasi-isotropic and not powered by a jet. However, the X-ray light curve can be well described by a simple power-law decay, i.e. no clear, ks-lasting plateau in the light curve is detected, such as has been previously invoked for FXTs that are suggested to be magnetar-powered (e.g. B. Zhang 2013; B. D. Metzger & A. L. Piro 2014; R. Ciolfi 2016; H. Sun et al. 2017, 2019; Y. Q. Xue et al. 2019; J. Quirola-Vásquez et al. 2024). Nevertheless, it is possible that our viewing angle to EP250207b is such that most of the plateau emission is not observed (the so-called 'trapped zone'; e.g. H. Sun et al. 2019). Only after the X-ray emission has ionized the ejecta in our line of sight the X-rays escape, leading to the detection of, in this case, a small part of the plateau (describing the *EP*-WXT light curve with a constant; see Fig. 1) and the power-law decay phase (cf. H. Sun et al. 2019; see Fig. 4).

The index of the best-fitting power-law decay of the X-ray light curve of -1.5 is in-between the predictions for the decay of $L_{\rm X} \propto t^{-1}$ and $L_{\rm X} \propto t^{-2}$ for times larger than the characteristic time-scale for magnetar spin-down due to the emission of gravitational wave (GW) radiation and for times larger than the characteristic time-scale for magnetar spin-down caused by electromagnetic radiation, respectively (cf. J. Quirola-Vásquez et al. 2024). However, the power-law index does not need to be -1 or -2, if the electromagnetic radiation from an ms magnetar is not only from vacuum dipole radiation. Moreover, the spin-down mechanism evolves with time. Therefore, given that the value of ≈ -1.5 is measured over a day- to week-long time period, it can also reflect this evolution (see e.g. P. D. Lasky et al. 2017; N. Sarin, P. D. Lasky & G. Ashton 2020).

We have used several kilonova (KN) models implemented in REDBACK (N. Sarin et al. 2024) to calculate possible KN optical (*F*606*W*) and NIR (*F*105*W*, *F*125*W*, and *F*160*W*) light curves to compare with the *HST* data points (see Fig. 11). We find that many of the KN models from D. Kasen et al. (2017) overpredict the observed *HST* magnitudes at observer times of 7.3–8.7 d after the source

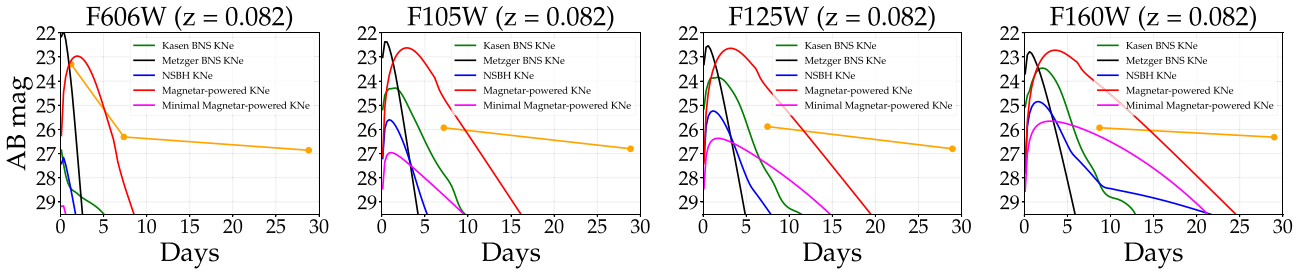

Figure 11. Plotted are the optical NIR data point in the filters as indicated and light curves for different KN models in the four main filters used in this work assuming a redshift $z = 0.082$. We follow D. Kasen et al. (2017) and B. D. Metzger (2017) for KN models, and we follow N. Sarin et al. (2022) for a magnetar-enhanced KN and a black hole–neutron star merger model. We use these models as implemented in REDBACK (N. Sarin et al. 2024; TWO_COMPONENT_NSBH_EJECTA_RELATION for the black hole–neutron star merger model) to calculate theoretical KN light curves in the optical (r'/$F606W$) and NIR ($F105W$, $F125W$, and $F160W$) filters. We find that if EP250207b is indeed at $z = 0.082$, only KN emission models with relatively low ejecta masses are consistent with the observed magnitudes (yellow symbols) at $t \approx 1.23, 7.4-8.7$ d. A typical magnetar-enhanced KN model is overpredicting the KN emission compared with the *HST*/WFC3 NIR data (red curve). Only an extreme version of a magnetar-enhanced KN is consistent with the data (magenta curve). The two data points at ≈7/28 d in each panel are the two *HST* measurements, the first data point in the *left* panel is the NOT r'-band measurement. Note that while the source is too bright to be explained by KN emission during the second epoch ($t \approx 28-29$ d), this could be explained if the source resides in a globular cluster or the core of a (tidally disrupted) dwarf galaxy. See text for details.

discovery. Only KN emission produced by mergers giving rise to a relatively low ejecta mass of 0.005 $M_\odot$ is consistent with the observations (green line in Fig. 11). The assumed lanthanide fraction is 10^{-1}. Such ejecta masses are low compared to the ejecta masses typically found from modelling the observations of GW 170817 (e.g. V. A. Villar et al. 2017; E. Waxman et al. 2018) and samples of short GRBs (e.g. J. C. Rastinejad et al. 2021). Also, while there are not many spectroscopically confirmed KNe known, such low ejecta masses are rarely seen in numerical simulations, which produce hypermassive or longer lived neutron stars (K. Kawana, A. Tanikawa & N. Yoshida 2018; K. Kawaguchi et al. 2022), i.e. the magnetars that have been invoked to explain some FXTs, and more likely points towards a binary neutron star merger where the remnant promptly collapsed into a black hole (V. Nedora et al. 2022). The latter tend to produce less ejecta, both dynamically and from the disc winds (e.g. D. M. Siegel 2019; N. Sarin & P. D. Lasky 2021).

The KN models from B. D. Metzger (2017) produce a bright KN signal that rapidly decays, and can just be consistent with the observations; e.g. for an ejecta mass of 0.01 $M_\odot$, ejecta velocity of $0.25c$, lanthanide fraction $\chi = 0.1$, velocity index $\beta = 3$ for $m_{\rm ejecta} \propto v^{-\beta}$, and a grey-opacity of $\kappa = 0.5$ corresponding to lanthanide-poor, 'blue' ejecta. Magnetar-enhanced KN models from N. Sarin et al. (2022) for typical parameter values overpredict the optical and NIR magnitudes (red line in Fig. 11). The magnetar-enhanced models can only be made consistent with the *HST* observations for rather constraining, probably even implausible, parameters (magenta line in Fig. 11). This model requires significant GW emission, which reduces the available rotational energy budget available for electromagnetic radiation, has a high γ-ray opacity to further reduce the available energy in optical, and finally, we force the opacity to be high, in contrast to expected opacities in the case of long-lived neutron star remnants (B. D. Metzger 2019).

Finally, for a redshift $z = 0.082$, we calculate using BILBY (G. Ashton et al. 2019) that any binary neutron star merger like GW 170817 would probably provide a marginal GW signal detection with an SNR of ≈9 in LIGO–Virgo–Kagra, i.e. below the conventional trigger threshold of an SNR of 12. If the event was instead due to a black hole–neutron star merger, the black hole mass and spin would have to have been such that there was (ample) of material outside the black hole's event horizon, implying that as the GW signal would be stronger than for a BNS merger, it might well have yielded a detection. The lack of such a detection suggests therefore that a black hole–neutron star merger is less likely as an origin for EP250207b. Combining the time and sky location of EP250207b with GW data will boost the confidence in any GW signal (cf. N. Sarin, P. D. Lasky & R. S. Nathan 2023).

Next, we consider an alternative scenario where the association with the candidate host galaxy, WISEA J111002.65−075211.9, is a mere chance alignment and the FXT must originate from (near) another host galaxy. The light detected in the second epoch of *HST* observations could be due to an unresolved background galaxy. At a magnitude of $F606W \approx 27$ and an offset of $\lesssim 1$ arcsec, the chance alignment probability for such a galaxy is ≈10 per cent (J. S. Bloom, S. R. Kulkarni & S. G. Djorgovski 2002), significantly larger than the chance alignment probability of $\lesssim 0.5$ per cent for WISEA J111002.65−075211.9 (D. B. Malesani et al. 2025). Nevertheless, if we assume that the second-epoch *HST* detections of the source are in fact due to the unresolved host galaxy, and we fit BAGPIPES (A. C. Carnall et al. 2018) and PROSPECTOR (B. D. Johnson et al. 2021) models to it, we obtain a photometric redshift $z_{\rm BP} = 3.0 \pm 0.5$, and $z_{\rm Prosp} = 3.5 \pm 0.7$. We have added a figure showing the best-fitting PROSPECTOR galaxy model to Appendix C (see Fig. C1). For a redshift $z = 3$, the *EP*-WXT 0.3–10 keV X-ray luminosity would become 2×10^{50} erg s^{-1}, which is a typical value for long GRBs (e.g. see M. G. Dainotti et al. 2016). The absolute magnitude would become rest-frame g'-band ≈−21.5, not out of the ordinary for a long GRB host galaxy at such a redshift (e.g. B. Schneider et al. 2022). Thus, besides the higher chance alignment, this scenario cannot be ruled out.

Finally, we also briefly consider as host of EP250207b the galaxy marked with an 'N' in Fig. 6 that lies in projection to the north of the candidate host lenticular galaxy. Using the Legacy Survey (A. Dey et al. 2019) magnitude converted to Vega mag and correcting for Galactic extinction, we have $R = 23.7$ at a separation of 5.8 arcsec with respect to the FXT. This leads to chance association probability of 32 per cent for the galaxy. Even though this is thus a likely chance alignment, we derived the redshift from its MUSE spectrum. Two clear emission lines are found at observed wavelengths of 8132.2 ± 0.3 and 8138.6 ± 0.4 Å. The wavelengths of these lines are consistent with those of the [O II] doublet at a redshift $z = 2.1824$. If EP250207b and its counterpart are in fact associated with this galaxy, the offset of the optical counterpart to the centre of this

galaxy of ≈5.78 arcsec corresponds to an offset of about 50 kpc in projection, still consistent with the distribution of offsets found for short GRBs (see references above) but inconsistent with the cumulative distribution for long GRBs (P. K. Blanchard, E. Berger & W.-f. Fong 2016). The observed peak absolute magnitude in the r' band would become −21.7, near the bright end of the short GRB distribution (see Fig. 9) and the average X-ray luminosity at the *EP*-WXT discovery $L_{\rm X} = 2 \times 10^{49}$ erg s^{-1} for this higher redshift. The radio $L_{3.06\ \rm GHz}$ would become $\lesssim 3 \times 10^{40}$ erg s^{-1}, or $\lesssim 9 \times 10^{30}$ erg s^{-1} Hz^{-1}. These values for the radio luminosity are in line with those found for other short GRBs (see e.g. fig. 13 in W. Fong et al. 2021). However, the peak X-ray luminosity in this case becomes too high to be a magnetar-powered FXT and we must be observing the jet-related prompt X-ray emission. Concluding, even if the galaxy marked 'N' is the host galaxy, this *EP*-discovered FXT can be explained as due to a merger-driven event and not as a collapsar-driven event.

ACKNOWLEDGEMENTS

We thank the referee for their comments, which helped improve the manuscript.

We are deeply grateful to Tom Marsh for developing the MOLLY software, one of his many contributions to advancing the field of compact objects.

PGJ, JNDvD, JS-S, JAQ-V, MER, and APCvH were supported by the European Union (ERC, Starstruck, 101095973, PI Jonker). Views and opinions expressed are, however, those of the author(s) only and do not necessarily reflect those of the European Union or the European Research Council Executive Agency. Neither the European Union nor the granting authority can be held responsible for them. DMS and MAPT acknowledge support by the Spanish Ministry of Science via the Plan de Generacion de conocimiento PID2020-120323GB-I00. DMS also acknowledges support via a Ramon y Cajal Fellowship RYC2023-044941. JAQ-V additionally acknowledges support by the IAU-Gruber foundation. SJS acknowledges funding from STFC grant ST/Y001605/1, a Royal Society Research Professorship, and the Hintze Charitable Foundation. DBM was funded by the European Union (ERC, HEAVYMETAL, 101071865). The Cosmic Dawn Center (DAWN) is funded by the Danish National Research Foundation under grant DNRF140. T-WC acknowledges the financial support from the Yushan Fellow Program by the Ministry of Education, Taiwan (MOE-111-YSFMS-0008-001-P1) and the National Science and Technology Council, Taiwan (NSTC grant 114-2112-M-008-021-MY3). FEB acknowledges support from ANID-Chile BASAL CATA FB210003, FONDECYT Regular 1241005, and Millennium Science Initiative, AIM23-0001. GL acknowledges support from a VILLUM FONDEN research grant (VIL60862). GPL was supported by a Royal Society Dorothy Hodgkin Fellowship (grant nos DHF-R1-221175 and DHF-ERE-221005). FO acknowledges support from MIUR, PRIN 2020 (grant 2020KB33TP) 'Multimessenger astronomy in the Einstein Telescope Era (METE)' and from INAF-MINIGRANT (2023): 'SeaTiDE – Searching for Tidal Disruption Events with ZTF: the Tidal Disruption Event population in the era of wide field surveys'.

This study is based on observations obtained at the international Gemini Observatory (Programme IDs GS-2024B-Q-131 and GS-2024B-FT-112), a programme of NOIRLab, which is managed by the Association of Universities for Research in Astronomy (AURA) under a cooperative agreement with the National Science Foundation on behalf of the Gemini Observatory partnership: the National Science Foundation (United States), National Research Council (Canada), Agencia Nacional de Investigación y Desarrollo (Chile), Ministerio de Ciencia, Tecnología e Innovación (Argentina), Ministério da Ciência, Tecnologia, Inovações e Comunicações (Brazil), and Korea Astronomy and Space Science Institute (Republic of Korea). Data were processed using the Gemini DRAGONS (Data Reduction for Astronomy from Gemini Observatory North and South) package.

Data for this paper have in part been obtained under the International Time Programme of the CCI (International Scientific Committee of the Observatorios de Canarias of the IAC) with the NOT and GTC operated on the island of La Palma by the Roque de los Muchachos.

The Legacy Surveys consist of three individual and complementary projects: the Dark Energy Camera Legacy Survey (DECaLS; Proposal ID #2014B-0404; PIs: David Schlegel and Arjun Dey), the Beijing-Arizona Sky Survey (BASS; NOAO Proposal ID #2015A-0801; PIs: Zhou Xu and Xiaohui Fan), and the Mayall z-band Legacy Survey (MzLS; Proposal ID #2016A-0453; PI: Arjun Dey). DECaLS, BASS, and MzLS together include data obtained, respectively, at the Blanco telescope, Cerro Tololo Inter-American Observatory, NSF's NOIRLab; the Bok telescope, Steward Observatory, University of Arizona; and the Mayall telescope, Kitt Peak National Observatory, NOIRLab. Pipeline processing and analyses of the data were supported by NOIRLab and the Lawrence Berkeley National Laboratory (LBNL). The Legacy Surveys project is honoured to be permitted to conduct astronomical research on Iolkam Duág (Kitt Peak), a mountain with particular significance to the Tohono Oódham Nation.

NOIRLab is operated by the Association of Universities for Research in Astronomy (AURA) under a cooperative agreement with the National Science Foundation. LBNL is managed by the Regents of the University of California under contract to the U.S. Department of Energy.

The data presented here were obtained (in part) with ALFOSC, which is provided by the Instituto de Astrofisica de Andalucia (IAA) under a joint agreement with the University of Copenhagen and NOT.

This project used data obtained with the Dark Energy Camera (DECam), which was constructed by the Dark Energy Survey (DES) collaborating institutions: Argonne National Lab, University of California Santa Cruz, University of Cambridge, Centro de Investigaciones Energeticas, Medioambientales y Tecnologicas-Madrid, University of Chicago, University College London, DES-Brazil consortium, University of Edinburgh, ETH-Zurich, University of Illinois at Urbana-Champaign, Institut de Ciencies de l'Espai, Institut de Fisica d'Altes Energies, Lawrence Berkeley National Lab, Ludwig-Maximilians Universitat, University of Michigan, National Optical Astronomy Observatory, University of Nottingham, Ohio State University, University of Pennsylvania, University of Portsmouth, SLAC National Lab, Stanford University, University of Sussex, and Texas A&M University. Funding for DES, including DECam, has been provided by the U.S. Department of Energy, National Science Foundation, Ministry of Education and Science (Spain), Science and Technology Facilities Council (UK), Higher Education Funding Council (England), National Center for Supercomputing Applications, Kavli Institute for Cosmological Physics, Financiadora de Estudos e Projetos, Fundação Carlos Chagas Filho de Amparo a Pesquisa, Conselho Nacional de Desenvolvimento Científico e Tecnológico and the Ministério da Ciência e Tecnologia (Brazil), the German Research Foundation-sponsored cluster of excellence "Origin and Structure of the Universe" and the DES collaborating institutions. The Collaborating Institutions are Argonne National Laboratory, the University of California at Santa Cruz, the University of Cambridge, Centro de Investigaciones Energeticas, Medioambientales y Tecnologicas-Madrid, the University of Chicago, University

College London, the DES-Brazil Consortium, the University of Edinburgh, the Eidgenossische Technische Hochschule (ETH) Zurich, Fermi National Accelerator Laboratory, the University of Illinois at Urbana-Champaign, the Institut de Ciencies de l'Espai (IEEC/CSIC), the Institut de Fisica d'Altes Energies, Lawrence Berkeley National Laboratory, the Ludwig Maximilians Universitat Munchen and the associated Excellence Cluster Universe, the University of Michigan, NSF's NOIRLab, the University of Nottingham, the Ohio State University, the University of Pennsylvania, the University of Portsmouth, SLAC National Accelerator Laboratory, Stanford University, the University of Sussex, and Texas A&M University.

BASS is a key project of the Telescope Access Program (TAP), which has been funded by the National Astronomical Observatories of China, the Chinese Academy of Sciences (the Strategic Priority Research Program 'The Emergence of Cosmological Structures' Grant # XDB09000000), and the Special Fund for Astronomy from the Ministry of Finance. The BASS is also supported by the External Cooperation Program of Chinese Academy of Sciences (Grant # 114A11KYSB20160057), and Chinese National Natural Science Foundation (Grant # 12120101003, # 11433005).

The Legacy Survey team makes use of data products from the Near-Earth Object Wide-field Infrared Survey Explorer (NEOWISE), which is a project of the Jet Propulsion Laboratory/California Institute of Technology. NEOWISE is funded by the National Aeronautics and Space Administration.

The Legacy Surveys imaging of the DESI footprint is supported by the Director, Office of Science, Office of High Energy Physics of the U.S. Department of Energy under Contract No. DE-AC02-05CH1123, by the National Energy Research Scientific Computing Center, a DOE Office of Science User Facility under the same contract; and by the U.S. National Science Foundation, Division of Astronomical Sciences under Contract No. AST-0950945 to NOAO.

The MeerKAT telescope is operated by the South African Radio Astronomy Observatory, which is a facility of the National Research Foundation, an agency of the Department of Science and Innovation. This work has made use of the 'MPIfR *S*-band receiver system' designed, constructed, and maintained by funding of the MPI für Radioastronomy and the Max Planck Society.

DATA AVAILABILITY

Data used in this paper are publicly available in the Zenodo repository (10.5281/zenodo.17579065).

REFERENCES

Abbott B. P. et al., 2017, Phys. Rev. Lett., 119, 161101
Alp D., Larsson J., 2020, ApJ, 896, 39
Arnaud K. A., 1996, in Jacoby G. H., Barnes J., eds, ASP Conf. Ser. Vol. 101, Astronomical Data Analysis Software and Systems V. Astron. Soc. Pac., San Francisco, p. 17
Aryan A. et al., 2025, ApJS, 281, 20
Ashton G. et al., 2019, ApJS, 241, 27
Bauer F. E. et al., 2017, MNRAS, 467, 4841
Berger E., Fong W., Chornock R., 2013, ApJ, 774, L23
Blanchard P. K., Berger E., Fong W.-f., 2016, ApJ, 817, 144
Blanton M. R., Roweis S., 2007, AJ, 133, 734
Bloom J. S., Kulkarni S. R., Djorgovski S. G., 2002, AJ, 123, 1111
Busmann M. et al., 2025, A&A, 701, A225
Cai C. et al., 2021, MNRAS, 508, 3910
Cai C. et al., 2025, Sci. China Phys. Mech. Astron., 68, 239511
Camilo F. et al., 2018, ApJ, 856, 180
Cappellari M., 2017, MNRAS, 466, 798
Cappellari M., Copin Y., 2003, MNRAS, 342, 345
Carnall A. C., McLure R. J., Dunlop J. S., Davé R., 2018, MNRAS, 480, 4379
CASA Team et al., 2022, PASP, 134, 114501
Cash W., 1979, ApJ, 228, 939
Cheng H. et al., 2024, Exp. Astron., 57, 10
Ciolfi R., 2016, ApJ, 829, 72
Conroy C., Gunn J. E., 2010, ApJ, 712, 833
Conroy C., Gunn J. E., White M., 2009, ApJ, 699, 486
Conroy C., White M., Gunn J. E., 2010, ApJ, 708, 58
Dainotti M. G., Postnikov S., Hernandez X., Ostrowski M., 2016, ApJ, 825, L20
Dey A. et al., 2019, AJ, 157, 168
Eappachen D. et al., 2023, ApJ, 948, 91
Eappachen D. et al., 2024, MNRAS, 527, 11823
Emsellem E. et al., 2004, MNRAS, 352, 721
ESO CPL Development Team, 2015, Astrophysics Source Code Library, record ascl:1504.003
Eyles-Ferris R. A. J. et al., 2025, ApJ, 988, L14
Fong W. et al., 2021, ApJ, 906, 127
Fong W.-f. et al., 2022, ApJ, 940, 56
Gianfagna G. et al., 2025, A&A, 703, A92
Gillanders J. H. et al., 2024, ApJ, 969, L14
Glennie A., Jonker P. G., Fender R. P., Nagayama T., Pretorius M. L., 2015, MNRAS, 450, 3765
Granot J., Piran T., 2012, MNRAS, 421, 570
Guevel D., Hosseinzadeh G., Bostroem A., Burke C. J., 2021, dguevel/PyZOGY: v0.0.2, Zenodo. Available at: https://doi.org/doi:10.5281/zenodo.4570234
Güver T., Özel F., 2009, MNRAS, 400, 2050
Harris W. E., 2010, preprint (arXiv:1012.3224)
Heywood I., 2020, Astrophysics Source Code Library, record ascl:2009.003
HI4PI Collaboration, 2016, A&A, 594, A116
Hjorth J. et al., 2003, Nature, 423, 847
Hugo B. V., Perkins S., Merry B., Mauch T., Smirnov O. M., 2022, in Ruiz J. E., Pierfedereci F., Teuben P., eds, ASP Conf. Ser. Vol. 532, Astronomical Data Analysis Software and Systems XXX. Astron. Soc. Pac., San Francisco, p. 541
Jiang S.-Q. et al., 2025, ApJ, 988, L34
Johnson B. D., Leja J., Conroy C., Speagle J. S., 2021, ApJS, 254, 22
Jonas J., 2018, Proc. Sci., The MeerKAT Radio Telescope. SISSA, Trieste, PoS(MeerKAT2016)001
Jonker P. G. et al., 2013, ApJ, 779, 14
Kann D. A. et al., 2010, ApJ, 720, 1513
Kann D. A. et al., 2011, ApJ, 734, 96
Kann D. A., Klose S., Zeh A., 2006, ApJ, 641, 993
Kasen D., Metzger B., Barnes J., Quataert E., Ramirez-Ruiz E., 2017, Nature, 551, 80
Kawaguchi K., Fujibayashi S., Hotokezaka K., Shibata M., Wanajo S., 2022, ApJ, 933, 22
Kawana K., Tanikawa A., Yoshida N., 2018, MNRAS, 477, 3449
Kouveliotou C., Meegan C. A., Fishman G. J., Bhat N. P., Briggs M. S., Koshut T. M., Paciesas W. S., Pendleton G. N., 1993, ApJ, 413, L101
Lamb G. P. et al., 2019, ApJ, 870, L15
Lamb G. P., Kobayashi S., 2019, MNRAS, 489, 1820
Lamb G. P., Mandel I., Resmi L., 2018, MNRAS, 481, 2581
Lasky P. D., Leris C., Rowlinson A., Glampedakis K., 2017, ApJ, 843, L1
Levan A. J. et al., 2014, ApJ, 781, 13
Levan A. J. et al., 2025, Nat. Aston., 9, 1375
Levan A. J., Malesani D. B., Jonker P. G., Quirola-Vásquez J. A., Sánchez-Sierras J., Martin-Carrillo A., Bauer F. E., 2025, GCN Circ., 39278, 1
Li X. Q. et al., 2022, Radiat. Detect. Technol. Methods, 6, 12
Lin D., Irwin J. A., Berger E., Nguyen R., 2022, ApJ, 927, 211
Lin D., Irwin J., Berger E., 2019, Astron. Telegram, 13171, 1
Liu Y. et al., 2025a, Nat. Astron., 9, 564
Liu X. et al., 2025b, GCN Circ., 39300, 1
Liu X. et al., 2025c, GCN Circ., 40260, 1
Lyman J. D. et al., 2018, Nat. Astron., 2, 751
Malesani D. B., Levan A. J., Quirola-Vasquez J. A., Jonker P. G., Sanchez-Sierras J., Bauer F., 2025, GCN Circ., 39270, 1

Mandhai S., Lamb G. P., Tanvir N. R., Bray J., Nixon C. J., Eyles-Ferris R. A. J., Levan A. J., Gompertz B. P., 2022, MNRAS, 514, 2716
Metzger B. D., 2017, Living Rev. Relativ., 20, 3
Metzger B. D., 2019, Living Rev. Relativ., 23, 1
Metzger B. D., Piro A. L., 2014, MNRAS, 439, 3916
Mieske S., Hilker M., Infante L., 2002, A&A, 383, 823
Nedora V. et al., 2022, Class. Quantum Gravity, 39, 015008
Nicholl M. et al., 2023, ApJ, 954, L28
Nicuesa Guelbenzu A. et al., 2012, A&A, 548, A101
Offringa A. R. et al., 2014, MNRAS, 444, 606
Planck Collaboration VI, 2020, A&A, 641, A6
Quirola-Vásquez J. et al., 2022, A&A, 663, A168
Quirola-Vásquez J. et al., 2023, A&A, 675, A44
Quirola-Vásquez J. et al., 2024, A&A, 683, A243
Quirola-Vásquez J. et al., 2025a, A&A, 695, A279
Quirola-Vasquez J. A. et al., 2025b, GCN Circ., 39733, 1
Quirola-Vásquez J, 2025c. MNRAS, available at: https://doi.org/10.1093/mnras/staf2064
Rastinejad J. C. et al., 2021, ApJ, 916, 89
Rastinejad J. C. et al., 2022, Nature, 612, 223
Rastinejad J. C. et al., 2025, ApJ, 988, L13
Ravasio M. E., Burns E., Jonker P. G., Fermi-GBM Team, 2025a, GCN Circ., 39269, 1
Ravasio M. E., Burns E., Jonker P. G., Fermi-GBM Team, 2025b, GCN Circ., 40703, 1
Ravasio M. E., Burns E., Jonker P. G., Hui M., Fermi-GBM Team, 2024, GCN Circ., 38435, 1
Sarin N. et al., 2024, MNRAS, 531, 1203
Sarin N., Lasky P. D., 2021, Gen. Relativ. Gravit., 53, 59
Sarin N., Lasky P. D., Ashton G., 2020, MNRAS, 499, 5986
Sarin N., Lasky P. D., Nathan R. S., 2023, MNRAS, 518, 5483
Sarin N., Omand C. M. B., Margalit B., Jones D. I., 2022, MNRAS, 516, 4949
Schlafly E. F., Finkbeiner D. P., 2011, ApJ, 737, 103
Schneider B., Le Floc'h E., Arabsalmani M., Vergani S. D., Palmerio J. T., 2022, A&A, 666, A14
Siegel D. M., 2019, Eur. Phys. J. A, 55, 203
Soderberg A. M. et al., 2008, Nature, 454, 246
Srinivasaragavan G. P. et al., 2025, ApJ, 988, L60
Srivastav S. et al., 2025, ApJ, 978, L21
Stanek K. Z. et al., 2003, ApJ, 591, L17
Sun H. et al., 2025, Nat. Astron., 9, 1073
Sun H., Li Y., Zhang B.-B., Zhang B., Bauer F. E., Xue Y., Yuan W., 2019, ApJ, 886, 129
Sun H., Zhang B., Gao H., 2017, ApJ, 835, 7
Tanvir N. R., Levan A. J., Fruchter A. S., Hjorth J., Hounsell R. A., Wiersema K., Tunnicliffe R. L., 2013, Nature, 500, 547
van Dalen J. N. D. et al., 2025, ApJ, 982, L47
Villar V. A. et al., 2017, ApJ, 851, L21
Wang C. et al., 2024, Exp. Astron., 57, 26
Waxman E., Ofek E. O., Kushnir D., Gal-Yam A., 2018, MNRAS, 481, 3423
Weilbacher P. M. et al., 2020, A&A, 641, A28
Wichern H. C. I., Ravasio M. E., Jonker P. G., Quirola-Vásquez J. A., Levan A. J., Bauer F. E., Kann D. A., 2024, A&A, 690, A101
Williams M. J., Veitch J., Messenger C., 2024, Astrophysics Source Code Library, record ascl:2405.002
Xue Y. Q. et al., 2019, Nature, 568, 198
Yadav M. et al., 2025, preprint (arXiv:2505.08781)
Yin Y.-H. I. et al., 2024, ApJ, 975, L27
Yuan W. et al., 2025, Sci. China Phys. Mech. Astron., 68, 239501
Yuan W., Zhang C., Chen Y., Ling Z., 2022, preprint (arXiv:2209.09763)
Zackay B., Ofek E. O., Gal-Yam A., 2016, ApJ, 830, 27
Zhang B., 2013, ApJ, 763, L22
Zhang D. et al., 2023, Nucl. Inst. Methods Phys. Res. A, 1056, 168586
Zhang W. et al., 2025a, Sci. China Phys. Mech. Astron., 68, 219511
Zhang Y.-Q. et al., 2025b, ApJ, 987, L38
Zhao X.-Y. et al., 2024, Res. Astron. Astrophys., 24, 104002
Zheng C. et al., 2025a, Sci. China Phys. Mech. Astron., 68, 271011
Zheng J.-H., Zhu J.-P., Lu W., Zhang B., 2025b, ApJ, 985, 21
Zhou X. Y., Li A., Zhao D. H., Xu X. P., Wu Q. Y., Liu Y., Einstein Probe Team, 2025, GCN Circ., 39266, 1
Zhu H., Tian W., Li A., Zhang M., 2017, MNRAS, 471, 3494

APPENDIX A: OPTICAL AND NIR PHOTOMETRY

Table A1. Optical and NIR photometry obtained through our follow-up observations. A > in front of the number in the AB magnitude column indicates a 3σ upper limit. The reported photometry is uncorrected for extinction, which taking the $N_{\rm H} = 4 \times 10^{20}$ cm^{-2} from the X-ray spectral fits would correspond to an $A_V = 0.18$ mag following T. Güver & F. Özel (2009).

Telescope (1)	Instrument (2)	Date (UTC) (3)	Days since trigger (4)	Exposure time (s) (5)	Filter (6)	AB magnitude (7)
NOT	ALFOSC	2025-02-09 03:16:13	1.228	4 × 200	r'	23.3 ± 0.16
NOT	NOTCam	2025-02-11 03:07:13	3.22	30 × 60	J	>22.8
GN	GMOS	2025-02-10 10:45:59	2.54	6 × 60	z'	24.7 ± 0.2
GN	GMOS	2025-02-11 11:25:46	3.57	5 × 60	g'	>24.7
GN	GMOS	2025-02-11 11:27:33	3.57	5 × 60	z'	>24.1
GS	GMOS	2025-02-12 06:23:32	4.36	12 × 60	z'	25.1 ± 0.3
GS	F2	2025-02-13 04:46:44	5.29	27 × 40	J	>24.2
GS	F2	2025-02-14 04:39:23	6.29	90 × 15	K_s	>23.15
HST	WFC3	2025-02-15 06:15:17	7.35	4 × 505	*F606W*	26.31 ± 0.08
HST	WFC3	2025-02-15 07:50:29	7.42	4 × 553	*F105W*	25.93 ± 0.02
HST	WFC3	2025-02-15 09:24:56	7.48	4 × 553	*F125W*	25.88 ± 0.11
HST	WFC3	2025-02-16 15:19:42	8.73	4 × 553	*F160W*	25.93 ± 0.15
HST	WFC3	2025-03-08 17:06:56	28.8	2 × 505	*F606W*	26.86 ± 0.15
HST	WFC3	2025-03-08 18:41:49	28.87	4 × 553	*F105W*	26.8 ± 0.2
HST	WFC3	2025-03-08 20:16:15	28.94	4 × 553	*F125W*	26.8 ± 0.2
HST	WFC3	2025-03-08 21:50:40	29	4 × 553	*F160W*	26.32 ± 0.18

APPENDIX B: AFTERGLOW MODELLING POSTERIOR DISTRIBUTION

APPENDIX C: PROSPECTOR MODELLING ASSUMING THAT *HST* SECOND-EPOCH DATA ARE DUE TO HOST

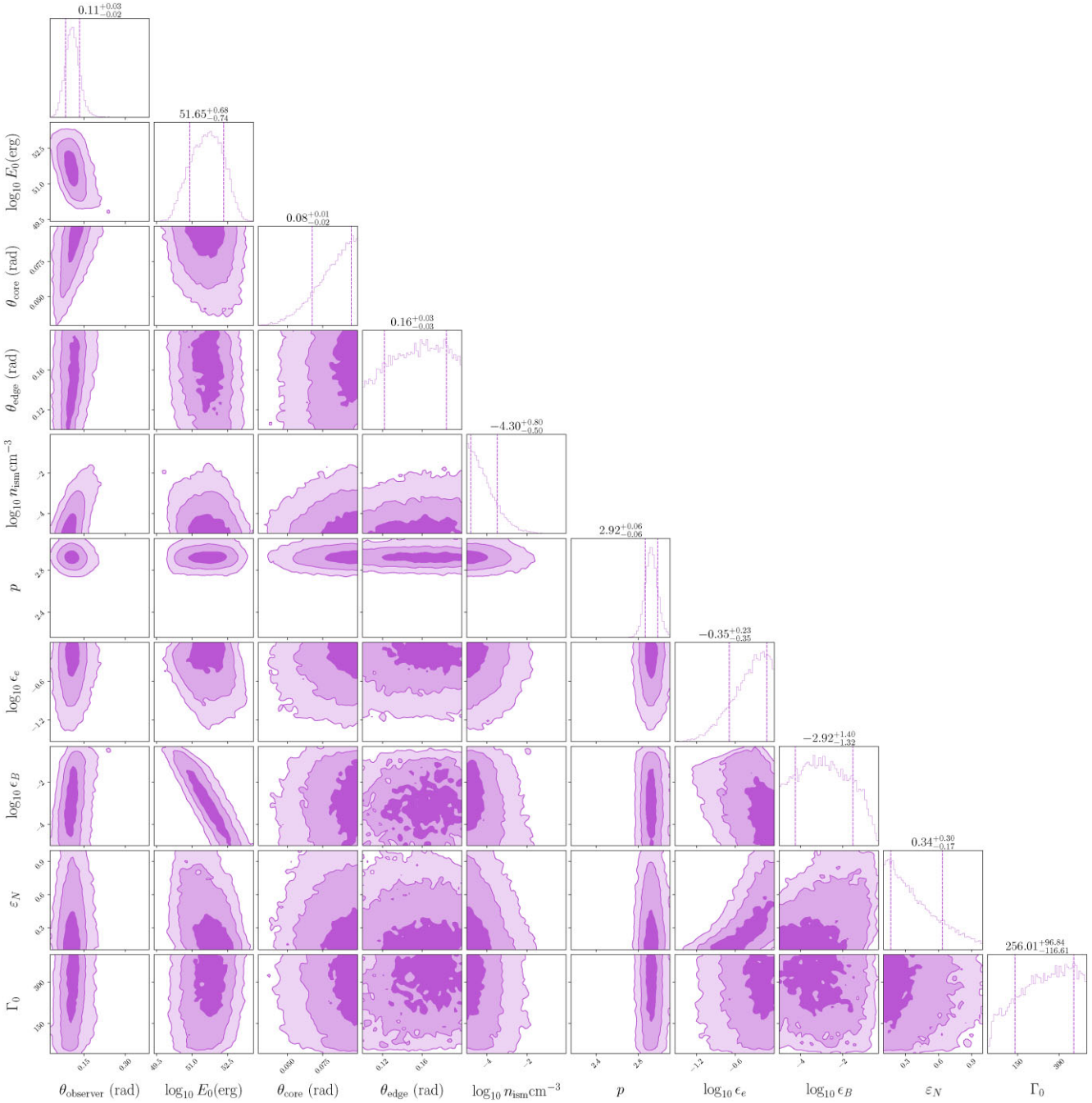

Figure B1. The posterior distribution for the model parameters used to fit the afterglow in Fig. 10. We excluded the optical and NIR data obtained after $t > 10$ d. The model fit used NESSAI as the sampler with a Gaussian likelihood via REDBACK. Parameter descriptions are given in Table 1.

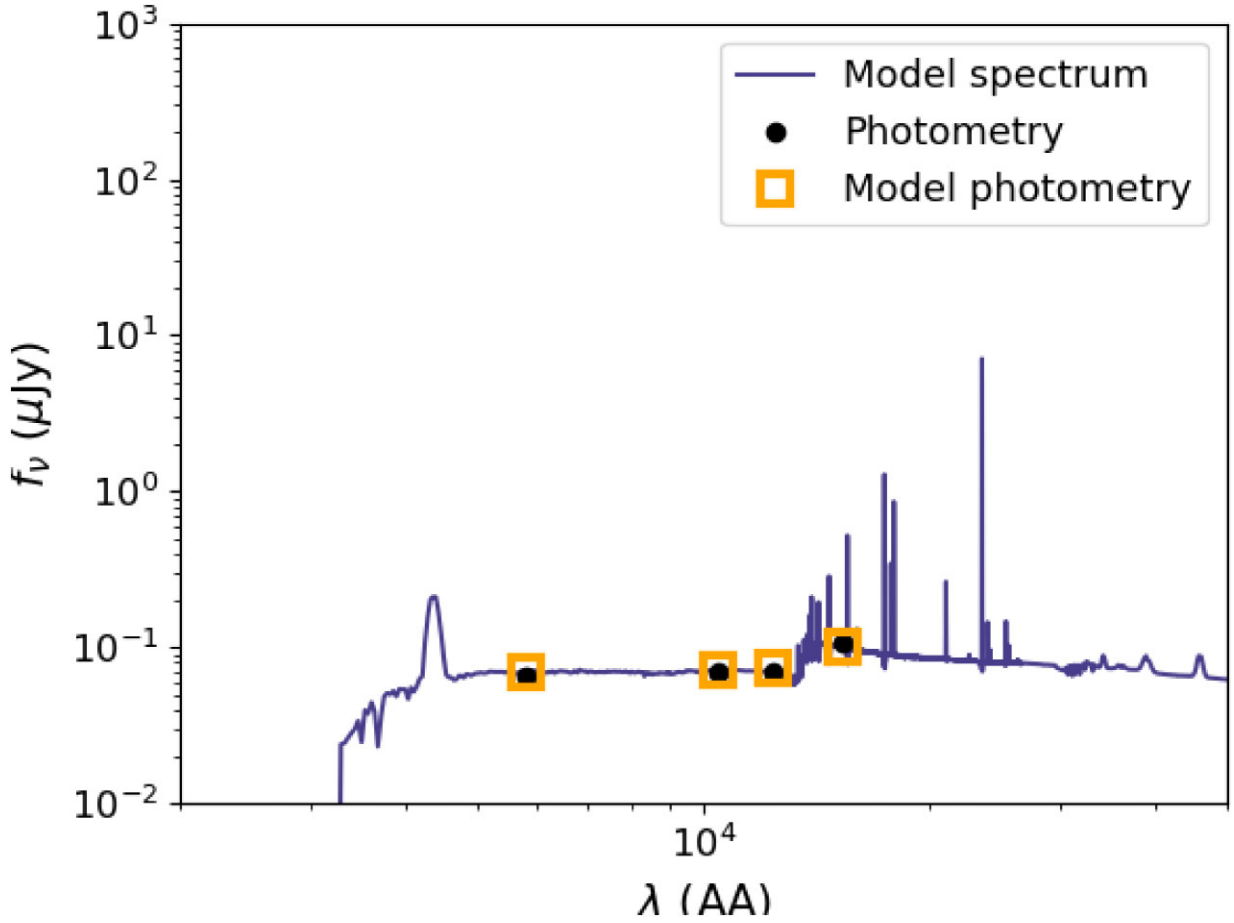

Figure C1. The best-fitting galaxy model obtained with PROSPECTOR is shown. The best-fitting parameters are redshift $z = 3.5 \pm 0.7$, metallicity $\log Z/Z_\odot = -1 \pm 0.7$, and mass of the galaxy formed in the most recent star formation episode $M_{\rm star} = (5^{+7}_{-4}) \times 10^9$ M$_\odot$. Currently, 60 per cent of this mass remains. The current star formation rate is 0.7 M$_\odot$ yr^{-1}. Note that there are systematic uncertainties, and we estimate that these are more important for the derived population age and metallicity than for the present-day stellar mass.

[1]*Department of Astrophysics/IMAPP, Radboud University, NL-6525 AJ Nijmegen, the Netherlands*
[2]*SRON, Netherlands Institute for Space Research, Niels Bohrweg 4, NL-2333 CA Leiden, the Netherlands*
[3]*Department of Physics, University of Warwick, Gibbet Hill Road, Coventry CV4 7AL, UK*
[4]*National Astronomical Observatories, Chinese Academy of Sciences, Beijing 100101, China*
[5]*School of Astronomy and Space Science, University of Chinese Academy of Sciences, Beijing 100049, China*
[6]*Beijing Normal University, No. 19, Xinjiekouwai St, Haidian District, Beijing 100875, China*
[7]*Kavli Institute for Cosmology, University of Cambridge, Madingley Road, CB3 0HA, Cambridge, UK*
[8]*Institute of Astronomy, University of Cambridge, Madingley Road, CB3 0HA, Cambridge, UK*
[9]*School of Physics and Astronomy, University of Leicester, University Road, LE1 7RH, Leicester, UK*
[10]*Astrophysics Research Institute, Liverpool John Moores University, IC2 Liverpool Science Park, 146 Brownlow Hill, Liverpool L3 5RF, UK*
[11]*Cosmic Dawn Center (DAWN), Denmark*
[12]*Niels Bohr Institute, University of Copenhagen, Jagtvej 128, DK-2200 Copenhagen N, Denmark*
[13]*Instituto de Alta Investigación, Universidad de Tarapacá, Casilla 7D, 1010000, Arica, Chile*
[14]*Instituto de Astrofísica, Facultad de Física, Pontificia Universidad Católica de Chile, Campus San Joaquín, Av. Vicuña Mackenna 4860, Macul Santiago 7820436, Chile*
[15]*Department of Physics, University of Oxford, Keble Road, Oxford OX1 3RH, UK*
[16]*Astrophysics Research Centre, School of Mathematics and Physics, Queen's University, Belfast BT7 1NN, UK*
[17]*School of Physics and Centre for Space Research, University College Dublin, Belfield, Dublin 4, D04 P7W1, Ireland*
[18]*Osservatorio di Astrofisica e Scienza dello Spazio, INAF, Via Piero Gobetti 93/3, I-40129 Bologna, Italy*
[19]*INAF-Osservatorio Astronomico d'Abruzzo, via M. Maggini snc, I-64100 Teramo, Italy*
[20]*DARK, Niels Bohr Institute, University of Copenhagen, Jagtvej 155A, DK-2200 Copenhagen, Denmark*
[21]*Graduate Institute of Astronomy, National Central University, 300 Jhongda Road, 32001 Jhongli, Taiwan*
[22]*DTU Space, Department of Space Research and Space Technology, Technical University of Denmark, Elektrovej 327, DK-2800 Kgs. Lyngby, Denmark*
[23]*Istituto Nazionale di Astrofisica INAF Osservatorio Astronomico di Padova via dell'Osservatorio 8, I-36012 Asiago, Italy*

[24]*Center for Interdisciplinary Exploration and Research in Astrophysics (CIERA), Northwestern University, 1800 Sherman Ave., Evanston, IL 60201, USA*
[25]*MIFT Department, University of Messina, via F. S. D'Alcontres 31, I-98166 Messina, Italy*
[26]*INAF-Osservatorio Astronomico di Roma, Via Frascati 33, I-00078 Monte Porzio Catone (RM), Italy*
[27]*Breakthrough Listen, Astrophysics, Department of Physics, The University of Oxford, Keble Road, Oxford OX1 3RH, UK*
[28]*State Key Laboratory of Particle Astrophysics, Institute of High Energy Physics, Chinese Academy of Sciences, 19B Yuquan Road, Beijing 100049, China*
[29]*Instituto de Astrofísica de Canarias, IAC, E-38205 La Laguna, Tenerife, Spain*
[30]*Departamento de Astrofísica, Univ. de La Laguna, E-38206 La Laguna, Tenerife, Spain*

This paper has been typeset from a TEX/LATEX file prepared by the author.